RESEARCH ARTICLE

Temperature Gradient Analyses of a Tubular Solid Oxide Fuel Cell Fueled by Methanol

Qidong Xu[1] · Meiting Guo[1] · Lingchao Xia[1] · Zheng Li[1] · Qijiao He[1] · Dongqi Zhao[1,2] · Keqing Zheng[3] · Meng Ni[1]

Abstract

Thermal management in solid oxide fuel cells (SOFC) is a critical issue due to non-uniform electrochemical reactions and convective flows within the cells. Therefore, a 2D mathematical model is established herein to investigate the thermal responses of a tubular methanol-fueled SOFC. Results show that unlike the low-temperature condition of 873 K, where the peak temperature gradient occurs at the cell center, it appears near the fuel inlet at 1073 K because of the rapid temperature rise induced by the elevated current density. Despite the large heat convection capacity, excessive air could not effectively eliminate the harmful temperature gradient caused by the large current density. Thus, optimal control of the current density by properly selecting the operating potential could generate a local thermal neutral state. Interestingly, the maximum axial temperature gradient could be reduced by about 18% at 973 K and 20% at 1073 K when the air with a 5 K higher temperature is supplied. Additionally, despite the higher electrochemical performance observed, the cell with a counter-flow arrangement featured by a larger hot area and higher maximum temperature gradients is not preferable for a ceramic SOFC system considering thermal durability. Overall, this study could provide insightful thermal information for the operating condition selection, structure design, and stability assessment of realistic SOFCs combined with their internal reforming process.

Keywords Solid oxide fuel cell · Modeling · Methanol fuel · Temperature gradient · Internal reforming

List of symbols

LSM	Lanthanum strontium manganate
MDR	Methanol decomposition reaction
SOFC	Solid oxide fuel cell
SCCM	Standard cubic centimeters per minute
TPB	Triple-phase boundary
WGSR	Water–gas shift reaction
YSZ	Yttria-stabilized zirconia

✉ Keqing Zheng
keqingzheng@cumt.edu.cn

✉ Meng Ni
meng.ni@polyu.edu.hk

1 Department of Building and Real Estate, Research Institute for Sustainable Urban Development (RISUD) & Research Institute for Smart Energy (RISE), The Hong Kong Polytechnic University, Hong Kong 999077, China

2 School of Artificial Intelligence and Automation, Key Laboratory of Image Processing and Intelligent Control, Huazhong University of Science and Technology, Wuhan 430074, China

3 School of Low-Carbon Energy and Power Engineering, China University of Mining and Technology, Xuzhou 221116, China

Roman

c	Concentration of gas mixture, mol/m^3
C_p	Heat capacity, J/(mol K)
D_{ij}	Binary diffusion coefficient of species i and j, cm^2/s
D_{ik}	Knudsen diffusion coefficient of species i, cm^2/s
D_{ij}^{eff}	Effective binary diffusion coefficient of species i and j, cm^2/s
E	Equilibrium Nernst potential, V
F	Faraday constant, 96,485 C/mol
h	Enthalpy of formation, kJ/mol
ΔH	Enthalpy change of formation, kJ/mol
i	Current density, A/m^2
i_0	Exchange current density, A/m^2
J_i	Molar diffusion flux of species i, $mol/(m^2 s)$
L_{cell}	Cell length, mm
M_i	Molecular weight of species i, kg/mol
N	Number of electrons transferred per electrochemical reaction
N_i	Molar flux of species i, $mol/(m^2 s)$
p	(Partial) Pressure, Pa
Q_e	Energy source, W/m^3
Q_m	Mass source, $kg/(m^3 s)$

r	Mean pore radius, m
R	Gas constant, 8.3145 J/(mol K)
R_r	Rate of chemical reaction, mol/(m^3 s)
R_i	Rate of generation or consumption of species i, mol/(m^3 s)
s	Entropy, J/(mol K)
ΔS	Entropy change, J/(mol K)
S_{TPB}	Specific surface area, m^2/m^3
T	Temperature, K
u	Molar-averaged velocity, m/s
U	Mass-averaged velocity, m/s
V	Volume fraction
y_i	Molar fraction of species i

Greek Letters

α	Charge transfer coefficient
ε	Porosity
η	Polarization, V
κ	Permeability, m^2
λ	Thermal conductivity, W/(m K)
μ	Dynamic viscosity of gas mixture, Pa s
μ_i	Dynamic viscosity of species i, Pa s
ρ	Mass concentration of gas mixture or the density, kg/m^3
σ	Electrical conductivity, S/m
τ	Tortuosity

Subscripts

a	Anode
act	Activation
c	Cathode
che	Chemical reaction
ele	Electrochemical reaction
g	Gas mixture
l	Ionic phase
s	Electronic phase
sol	Solid phase

Superscripts

Eff	Effective
L	Local

Introduction

The solid oxide fuel cell (SOFC) is a promising future energy device since electricity can be electrochemically generated from the chemical energy of fuels through SOFCs with higher efficiency and lower greenhouse gas emission in comparison to traditional thermal power plants [1]. SOFCs are typically operated at high temperatures (873–1273 K) to maintain moderate oxygen ion conductivity of ceramic electrolytes [2], thus offering various beneficial aspects to the SOFC systems. For example, cheaper nickel (Ni) metal

could be utilized as the chemical/electrochemical catalyst in SOFCs, rendering a more economical prospect than proton-exchange membrane fuel cells (PEMFCs) [3–5]. Besides, the utilization of hydrocarbon [6, 7], alcohols [8], ammonia [9, 10], biomass [11], or even solid carbon [12, 13] in SOFCs is possible for power generation because these fuel sources can be internally reformed into more effective fuels (H$_2$ and CO) for faradic processes under the anodic environment [14]. The internal reforming process provides SOFCs with an efficient and sustainable operation since the thermal coupling of endothermic reforming and exothermic processes can improve the cell efficiency [15], and the integration of renewable fuel productions with direct hydrocarbon or alcohol SOFCs is promising in achieving carbon–neutral power generation. Moreover, given the considerable amount of waste heat produced due to cell inefficiency, accounting for 20–50% LHV (Lower heating value) of fuels [16], exhausted gases could be further used for bottoming cycles to generate extra power, maximizing overall system efficiency [17, 18].

However, despite the numerous benefits involved in the SOFC system, thermal management has been a major challenge [19]. Owing to the uneven electrochemical reactions and heat transfer of gas convective flows, non-uniform temperature distributions were frequently observed within the SOFC assembly or stack, especially for the internal reforming SOFCs, posing a threat to material deterioration and structural integrity. Local temperatures higher than the design value could lead to nickel coarsening because of the relatively low melting temperature of nickel and thermally favorable sintering process [20], degrading anode functions and consequently lowering the cell performance. For example, electrode sintering was observed at the bottom part of a tubular SOFC operated on the methane flame mode as the temperature of the corresponding position reached 1300 K [21]. Another thermal issue of temperature gradient arising from the non-uniform temperature distribution negatively affects the cell structure, thus cracking or delaminating brittle ceramic components that are more vulnerable under tensile stress [22]. For example, delaminations between the electrolyte and the electrode as well as cracks in the electrolytes were found in experimental tests due to the temperature gradient [21, 23], likely resulting in the complete failure of SOFCs as their components cannot be replaced or repaired [24]. Therefore, under the complicated thermal environment of SOFCs, the cell components are subjected to the accelerated rate of property evolution and degradation, eventually causing the fuel cell failure.

To solve the aforementioned problems, various efforts have been devoted to developing effective temperature control strategies in recent years. Zeng et al. [21] experimentally fabricated a tubular SOFC with a liquid-sodium heat pipe to equalize the temperature distribution. It was found that with the help of high thermal conductivity induced by

the evaporation–transport–condensation process in liquid sodium, the axial temperature gradient was significantly decreased, enhancing the cell electrochemical performance and life span. Dillig et al. [16] and Marocco et al. [25] have drawn similar conclusions in their simulation investigations. Recently, Promsen et al. [26] proposed a novel concept of SOFC cooled by saturated water. The calculation results indicated that the water-cooled stack demonstrated a better performance due to a more uniform temperature profile. Besides, due to the efficient cooling of the saturated water, the air flow was greatly reduced since conventionally heat dissipation in an SOFC is conducted by oversupplying cathode gas, decreasing the parasitic loads related to air preheating and blower energies. Combining an SOFC with a heat pipe or a water cooling tube enhances the temperature uniformity and electrochemical performance of a cell and reduces the costs related to auxiliary devices. However, the manufacturing cost and system complexity remain a challenge, especially for the SOFC stacks, as numerous heat pipes must be fabricated to achieve sufficient cooling effect [25]. Besides, possible leakage of liquid metal from the heat pipe might catastrophically damage the cell system given the complicated gas environment and chemically reactive nature of the liquid metal. Based on the same approach of increasing the thermal conductivity of solid cell components, utilization of metal support [27, 28], metallic interconnect [29], or metal cathode flow distributor [30] in SOFC fabrication also exhibited a more uniform temperature distribution, leading to improved cell stability in terms of thermal stress [29]. However, as indicated from the numerical study conducted by Park et al. [31], the bonding layer between the ceramic cell and the metallic support resisted hydrogen mass transfer, resulting in a 17% decrease in the average current density compared to the cermet anode-supported SOFC. Besides, possible metal oxidation risk [32], accelerated poisoning of cathode catalyst by Cr from ferritic stainless steel [33],

as well as relatively poor electrochemical performance [34] have limited the commercialization of this technology.

However, despite numerous theoretical and experimental works conducted with a focus on thermal control and management, to the best of our knowledge, a detailed thermo–electrochemical simulation has not been performed to identify the thermal characteristics, especially the temperature gradient profile of SOFC operated on methanol fuel. Importantly, unlike the battery, SOFC is an open system that thermally interacts with reacting gases; thus, the cell thermal state can be considerably influenced by gas conditions [35], especially for cathode air, but the cooling effects and thermal/electrical responses of air conditions have not been fully understood yet. Therefore, to fill this research gap, a validated mathematic model extended from our previous simulation works [36, 37] is developed to further investigate the temperature gradient profiles in cell components, especially ceramic electrolytes. This work will be critically essential for the operating condition selection, structure design, and failure assessment of realistic SOFCs.

Model Development

Working Principles and Modeling Assumptions

A fuel mixture of methanol and steam (molar ratio 1:1) is supplied into the fuel channel to electrochemically generate electricity. As shown in Fig. 1, the computation domain thermally consists of the anode and cathode channels, porous Ni-YSZ and YSZ–LSM composite electrodes, as well as dense YSZ electrolyte [38]. Macro- and micro-structural parameters, as well as the physical properties of materials adopted in the present study, are summarized in Tables 1 and 2, respectively.

Methanol is used as the primary fuel in this study due to its several promising features, such as storage/transportation

Fig. 1 Diagram of an anode-supported SOFC fed by the fuel mixture of methanol/steam
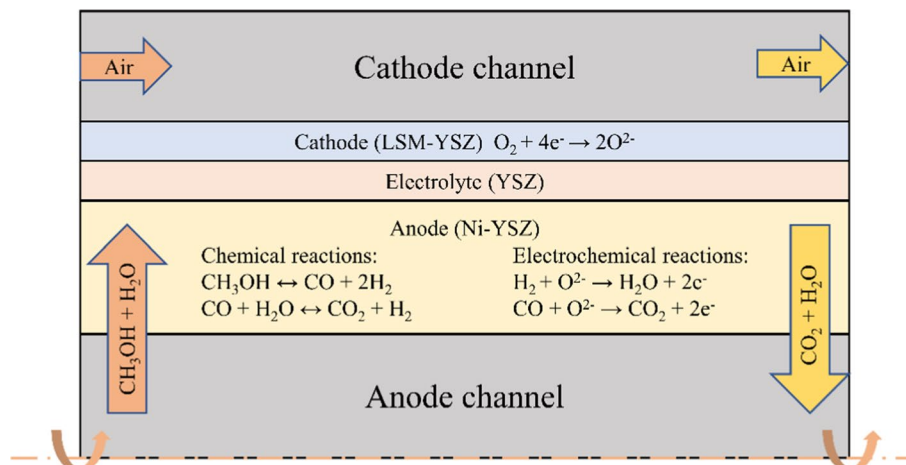
Table 1 Macro- and micro-structural parameters employed in the simulation

Parameter	Expression or value	Unit
Porosity		
Cathode	0.46	
Anode	0.46	
Permeability		
Cathode	1.76×10^{-11}	m^2
Anode	1.76×10^{-11}	m^2
Specific surface area		
Cathode	3.33×10^5	m^2/m^3
Anode	2.66×10^5	m^2/m^3
Thickness		
Cathode channel	2	mm
Cathode	0.1	mm
Electrolyte	0.01	mm
Anode	0.6	mm
Anode channel	2	mm
Cell length	6	cm
Tortuosity of electrodes	3	

Table 2 Physical properties of the materials [71, 72]

Parameter	Expression or value	Unit
Ionic conductivity		
YSZ	$3.34 \times 10^4 \times e^{\frac{-10300}{T}}$	S/m
Electronic conductivity		
Nickel	$3.27 \times 10^6 - 1065.3 \times T$	S/m
LSM	$4.2 \times 10^7/T \times e^{\frac{-1150}{T}}$	S/m
Heat capacity		
Cathode	398	J/(mol•K)
Electrolyte	525	J/(mol•K)
Anode	390	J/(mol•K)
Thermal conductivity		
Cathode	3.47	W/(m•K)
Electrolyte	2.57	W/(m•K)
Anode	6.23	W/(m•K)
Density		
Cathode	3814.8	kg/m^3
Electrolyte	6086	kg/m^3
Anode	6870	kg/m^3

conveniences [39], relatively high volumetric energy density [40], and significantly low coking threat [8]. To further eliminate carbon formation in cell operation, an equimolar amount of steam is added to the main methanol stream [6, 14]. Importantly, under the active catalytic effect of nickel, methanol could be readily converted into a H_2 and CO mixture through the methanol decomposition reaction (MDR, Eq. (1)), followed by water gas shift reaction (WGSR, Eq. (2)) to further generate H_2 in the presence of water [39]. At the anode functional layer, the generated H_2 and CO could be oxidized into H_2O and CO_2 by oxygen ions (Eqs. (3) and (4)), produced at the cathode side (Eq. (5)) and subsequently transported to the anode through an electron-insulated electrolyte. Electrons generated from electrochemical oxidation reactions can be conducted to the cathode layer via an external circuit producing electrical power.

$$CH_3OH \leftrightarrow CO + 2H_2 \qquad (1)$$

$$CO + H_2O \leftrightarrow CO_2 + H_2 \qquad (2)$$

$$H_2 + O^{2-} \rightarrow H_2O + 2e^- \qquad (3)$$

$$CO + O^{2-} \rightarrow CO_2 + 2e^- \qquad (4)$$

$$O_2 + 4e^- \rightarrow 2O^{2-} \qquad (5)$$

Based on the working mechanism, assumptions adopted in the simulation are listed below:

(1) Due to kinetically fast reaction rates, only hydrogen and carbon monoxide could be electrochemically oxidized.
(2) Local temperature equilibrium hypothesis is applied for porous electrodes because of the negligible temperature difference in the gas/solid phases [41].
(3) Heat conduction and convection transfers are considered.
(4) An incompressible laminar flow regime is used for bulk fuel and air flows.
(5) Gases simulated are treated as ideal gases.
(6) The evenly dispersed electrochemical/chemical reaction sites are assumed in both electrodes, and continuous and homogeneous ionic/electronic conductions are adopted.

Governing and Constitutive Equations

Based on the chemical/physical processes within the cell, five sub-models will be calculated simultaneously to elucidate the thermo–electrochemical environment of methanol-fueled tubular SOFC.

Chemical Reaction Model

Chemical reaction rates and heat changes could be calculated by the chemical reaction model. As a result of the active catalytic activity of Ni, MDR, and WGSR will principally occur at the porous anode [42]. The corresponding reaction rates (R_r) could be expressed by [43, 44]:

$$R_{\text{MDR}} = k_{\text{D}} p_{\text{CH}_3\text{OH}}^{\text{l}} E_{\text{qD}} \tag{6}$$

$$E_{\text{qD}} = 1 - \frac{p_{\text{CO}}^{\text{l}}\left(p_{\text{H}_2}^{\text{l}}\right)^2}{K_{\text{eq,D}} p_{\text{CH}_3\text{OH}}^{\text{l}}} \tag{7}$$

$$K_{\text{eq},D} = 1.718 \times 10^{14} \times e^{-\frac{95419}{RT}} \tag{8}$$

$$R_{\text{WGSR}} = k_{\text{sf}}\left(p_{\text{H}_2\text{O}}^{\text{l}} p_{\text{CO}}^{\text{l}} - \frac{p_{\text{H}_2}^{\text{l}} p_{\text{CO}_2}^{\text{l}}}{K_{\text{ps}}}\right) \tag{9}$$

$$k_{\text{sf}} = 0.0171 \times e^{-\frac{103191}{RT}} \tag{10}$$

$$K_{\text{ps}} = e^{(-0.2935Z^3 + 0.6351Z^2 + 4.1788Z + 0.3169)} \tag{11}$$

$$Z = \frac{1000}{T(\text{K})} - 1 \tag{12}$$

where T and p_i^{l} represent temperature and species local partial pressure, respectively; R denotes the universal gas constant, and tuning parameter k_{D} is used to validate the model.

Chemical reactions could lead to heat generation or consumption according to thermodynamics; thus, total chemical heat changes (Q_{che}) are determined by both reaction enthalpy changes of formation (ΔH) and rates, as shown below:

$$Q_{\text{che}} = R_{\text{MDR}} \Delta H_{\text{MDR}} + R_{\text{WGSR}} \Delta H_{\text{WGSR}} \tag{13}$$

$$\Delta H_{\text{MDR}} = 2h_{\text{H}_2} + h_{\text{CO}} - h_{\text{CH}_3\text{OH}} \tag{14}$$

$$\Delta H_{\text{WGSR}} = h_{\text{CO}_2} + h_{\text{H}_2} - h_{\text{CO}} - h_{\text{H}_2\text{O}} \tag{15}$$

$$h_i(T) = h_i(T_0) + \int_{T_0}^{T} C_{\text{p},i}(T)\text{d}T \tag{16}$$

where h_i and $C_{\text{p},i}$ denote the species enthalpy of formation and heat capacity, respectively.

Electrochemical Reaction Model

Electrical output and reversible/irreversible heat generations related to the electrochemical processes are determined by the electrochemical reaction model. The current density is described by the general Butler–Volmer (BV) equation (Eq. (17)), wherein the activation overpotential (η_{act}) reflects the electrochemical activation barrier [45].

$$i = i_0 e^{\frac{\alpha nF\eta_{\text{act}}}{RT}} - e^{\frac{-(1-\alpha)nF\eta_{\text{act}}}{RT}} \tag{17}$$

Here, α, n, and F are the charge transfer coefficient, the number of electrons for one single electrochemical reaction, and the Faraday constant, respectively; i_0 represents the exchange current density. In the present model, both H_2 and CO are oxidized, and the electrochemical rate of hydrogen oxidation is faster than that of carbon monoxide [42]; thus, i_0 is set as 2000, 3000, and 5300 A/m^2 for O_2, CO, and H_2, respectively. Because of various overpotential losses, the output potential (V, Eq. (18)) could be much lower than the thermodynamic equilibrium potential (E, Eqs. (19) and (20)), especially under high current density conditions.

$$V = E - \eta_{\text{act,a}} - \eta_{\text{act,c}} - \eta_{\text{ohmic}} \tag{18}$$

$$E_{\text{H}_2} = E_{\text{H}_2}^T + \frac{RT}{2F}\ln\left[\frac{p_{\text{H}_2}^{\text{l}}\left(p_{\text{O}_2}^{\text{l}}\right)^{0.5}}{p_{\text{H}_2\text{O}}^{\text{l}}}\right] \tag{19}$$

$$E_{\text{CO}} = E_{\text{CO}}^T + \frac{RT}{2F}\ln\left[\frac{p_{\text{CO}}^{\text{l}}\left(p_{\text{O}_2}^{\text{l}}\right)^{0.5}}{p_{\text{CO}_2}^{\text{l}}}\right] \tag{20}$$

$$E_{\text{H}_2}^T = 1.253 - 0.00024516 \times T \tag{21}$$

$$E_{\text{CO}}^T = 1.46713 - 0.0004527 \times T \tag{22}$$

In addition to the activation overpotential, ohmic overpotentials for ionic/electronic transport resistances can be calculated by Eqs. (23) and (24) according to Ohm's law [46].

$$i_{\text{l}} = -\sigma_{\text{l}}^{\text{eff}}\nabla(\emptyset_{\text{l}}) \tag{23}$$

$$i_{\text{s}} = -\sigma_{\text{s}}^{\text{eff}}\nabla(\emptyset_{\text{s}}) \tag{24}$$

Here, $\emptyset$ and σ^{eff} represent the phase potential and effective conductivity, respectively. During the electricity output, heat is released simultaneously, involving reversible electrochemical heat generation (Q_{ele}) due to change of entropy, irreversible joule heating (Q_{ohmic}) because of transport of charged species, and irreversible heat generation (Q_{act}) upon activation polarization [19]. Therefore, corresponding equations can be written as:

$$Q_{\text{ele}} = \frac{i_{\text{H}_2} T\Delta S_{\text{H}_2}}{2F} + \frac{i_{\text{CO}} T\Delta S_{\text{CO}}}{2F} \tag{25}$$

$$T\Delta S = \Delta H - \Delta G \tag{26}$$

$$\Delta S_{H_2} = s_{H_2O} - 0.5 s_{O_2} - s_{H_2} \tag{27}$$

$$\Delta S_{CO} = s_{CO_2} - 0.5 s_{O_2} - s_{CO} \tag{28}$$

$$s(T) = s(T_0) + \int_{T_0}^{T} \frac{C_p(T)}{T} dT \tag{29}$$

$$Q_{ohmic} = \frac{i^2}{\sigma^{eff}} \tag{30}$$

$$Q_{act} = i\eta_{act} \tag{31}$$

Computational Fluid Dynamics Model

Fuel and gas flows described by the velocity (U) and pressure (p) fields in electrodes and gas channels will be simulated by the computational fluid dynamics (CFD) model. In CFD, gas behaviors in the channels can be described by general continuity and Navier–Stokes (NS) equations (Eqs. (32) and (33)) [47]. However, in fuel and air electrodes, the modified continuity equation (Eq. (34)) with a mass source term and modified NS equation (Eq. (35)) with Darcy's term account for the mass exchange and porous microstructure, respectively [48].

$$\rho \nabla \cdot U = 0 \tag{32}$$

$$\rho(U \cdot \nabla) \cdot U = -\nabla p + \nabla \cdot \left[\mu \left(\nabla U + \nabla U^T \right) \right] \tag{33}$$

$$\rho \nabla \cdot U = Q_m \tag{34}$$

$$\begin{aligned} \frac{1}{\varepsilon} \rho (U \cdot \nabla) \cdot U \frac{1}{\varepsilon} = -\nabla p + \\ \nabla \cdot \left[\mu \frac{1}{\varepsilon} \left(\nabla U + \nabla U^T \right) - \frac{2}{3} \mu \frac{1}{\varepsilon} (\nabla \cdot U) \right] \\ - \left(\mu \kappa^{-1} + \frac{Q_m}{\varepsilon^2} \right) U \end{aligned} \tag{35}$$

Here, ε and κ represent the porosity and permeability of electrodes, respectively; Q_m is the net mass change; the dynamic viscosity (μ, Eq. (36)) of the gas mixture is estimated based on the species molecular weight (M_i) and molar fraction (y_i).

$$\mu = \sum_{i=1}^{n} \frac{y_i \mu_i}{\sum_{j=1}^{n} \left(y_i \sqrt{\frac{M_j}{M_i}} \right)} \tag{36}$$

Mass Transfer Model

Owing to various physical/chemical processes in an SOFC, the mass transfer model is used to calculate the species concentration distributions via steady-state species molar conservation equations with and without a source term applied in electrodes (Eq. (38)) and channels (Eq. (37)), respectively.

$$\nabla \cdot J_i + c(u \cdot \nabla) y_i = 0 \tag{37}$$

$$\nabla \cdot J_i + c(u \cdot \nabla) y_i = R_i \tag{38}$$

Here, R_i and J_i are the molar change rate and molar diffusion flux of species i, respectively; u and c represent the molar average velocity and molar concentration of the gas mixture, respectively. Molar diffusion flux in the species molar conservation equations could be estimated by the Stefan–Maxwell approach (Eqs. (39) and (40)) [49]. Notably, the effective binary diffusion coefficient (D_{ij}^{eff}, Eq. (42)) corrected by molecular and Knudsen diffusions, as well as microstructure [50] is used in porous electrodes [51], while only binary diffusion coefficient (D_{ij}), which can be determined by Eq. (41) [52, 53] is considered in gas channels. As claimed by the kinetic theory [54], the Knudsen diffusion coefficient (D_{ik}) could be expressed as Eq. (43).

$$\sum_{j=1, j\neq i}^{n} \frac{y_j N_i - y_i N_j}{D_{ij}} = -c \frac{dy_i}{dx} \tag{39}$$

$$\sum_{j=1, j\neq i}^{n} \frac{y_j N_i - y_i N_j}{D_{ij}^{eff}} = -c \frac{dy_i}{dx} \tag{40}$$

$$D_{ij} = \frac{0.00143 T^{1.75}}{2p \left(v_i^{1/3} + v_j^{1/3} \right)^2} \left(\frac{1}{M_i} + \frac{1}{M_j} \right)^{1/2} \tag{41}$$

$$D_{ij}^{eff} = \frac{\varepsilon}{\tau} \left(\frac{1}{D_{ij}} + \frac{1}{D_{ik}} \right)^{-1} \tag{42}$$

$$D_{ik} = \frac{2}{3} r \sqrt{\frac{8RT}{\pi M_i}} \tag{43}$$

Heat Transfer Model

Thermal characteristics within the entire computational domain can be described by the heat transfer model. To demonstrate the complicated thermal processes in an SOFC, general energy conservation equations with and without a heat source term are applied in electrodes (Eq. (45)) and gas

Table 3 Working conditions for the parametric simulation

Parameters	Value	Unit
Cathode gas flow rate	120–2400	SCCM
Cathode gas composition	O_2/N_2 (21%/79%)	
Anode flow rate (liquid)	0.2	mL/min (std)
Anode gas composition	H_2O/CH_3OH (molar ratio: 1/1)	
Inlet temperature	873–1113	K
Operating potential	0.5–0.9	V
Operating pressure	1	atm

channels (Eq. (44)), respectively. Besides, the mole fraction averaging method is used to estimate both the heat capacity (C_p, Eq. (46)) and thermal conductivity (λ_g, Eq. (47)) of a gas mixture [52, 55]. The gas species thermodynamic properties could be found in our previous publication [36].

$$\rho C_p u \cdot \nabla T + \nabla \cdot \left(-\lambda_g \nabla T\right) = 0 \tag{44}$$

$$\rho C_p u \cdot \nabla T + \nabla \cdot \left(-\lambda_{eff} \nabla T\right) = Q_e \tag{45}$$

$$C_p = \sum_{i=1}^{n} y_i C_{p,i} \tag{46}$$

$$\lambda_g = \sum_{i=1}^{n} y_i \lambda_i \tag{47}$$

$$\lambda_{eff} = (1-\varepsilon)\lambda_{sol} + \varepsilon \lambda_g \tag{48}$$

Mathematical Method and Operating Conditions

The developed model is simulated by solving fully-coupled nonlinear equations through the finite element method with a relative tolerance of 10^{-3}. To ensure grid independence, the model is composed of 30, 150, 10, 40, and 30 elements for anode channel, anode, electrolyte, cathode, and cathode channel widths, respectively, as well as 200 for cell length, generating 52,000 elements. Besides, the validation is conducted by comparing the calculated polarization curves with the experimental data [34], which can be readily found in our published studies [32, 33]. Working conditions for the following parametric calculation are given in Table 3.

Results and Discussion

Effects of Air Flow Rate

Calculations are employed to examine the effects of the air flow rate on tubular cell thermal/electrical performance

under several typical operating temperatures. Here, the operating potential is set as 0.5 V because although a large current density or a low operating potential is not desired in practical operations, negative thermal features can become quite obvious under a considerably high current density.

Current densities (Fig. 2a) can be highly influenced by the air flow rate. At a relatively low flow rate, current densities are nearly the same under different temperature conditions and considerably increase as the air flow rate increases. It is mainly because the cell performance is restricted by an insufficient oxygen supply for electrochemical reactions, evident from the complete consumption of oxygen (Fig. 2b), especially near the cathode outlet (Fig. 2c). With a further increase to 1200 SCCM, the current density at 1073 K continues to enhance slightly, while the power outputs for three relatively low-temperature conditions experience a gradual drop when the flow rate approximately exceeds a certain air flow rate (240 SCCM for 873 K, 500 SCCM for both 923 K and 973 K). These two different trends in cell performance are reasonable since relevant phenomena are found in the available literature. With the increase in the air flow rate or air ratio, a decreased cell performance was frequently observed in several simulation studies from Xu et al. (973 K) [56] and Li et al. (973 K) [57], while enhanced power densities were also achieved with the rise of air flow rate in the research works by Colpan et al. (1173 K) [58] and Raj et al. (1073 K) [59]. The possible reason for these two opposite phenomena is because of different cell sensitivities to the temperature change. At low operating temperatures, the cell performance is more sensitive to temperature variation, as indicated in Fig. 2a, where a temperature increase by 50 K from 873 K leads to a substantial current density improvement (about 5800 A/m^2), while the cell electrochemical performance at 1073 K is just 1400 A/m^2 higher compared to that at 973 K. Therefore, despite the increased oxygen concentration and thus decreased overpotential, the decrease in the cell average temperature (Fig. 2d) caused by the cooling air dominates the power output at 873 K, 923 K, and 973 K, reducing the cell performance. Conversely, a high operating temperature weakens the negative effect of the average temperature decrease, resulting in an insignificant but continuous increase in the power output when the air flow rate is faster than 500 SCCM at 1073 K.

In addition, the air flow rate can strongly impact the cell thermal characteristics involving axial temperature gradient and temperature distributions in the ceramic electrolyte (Fig. 3a, b). At 873 K, a peak temperature gradient approximately occurs at the center of the electrolyte because of the relatively moderate current density (Fig. 2a) and a smooth increase in temperature along the cell length near the gas inlet (Fig. 3a). Although limited by the inadequate oxygen and low chemical/electrochemical kinetics due to a slow air flow and a low operating temperature, respectively, the
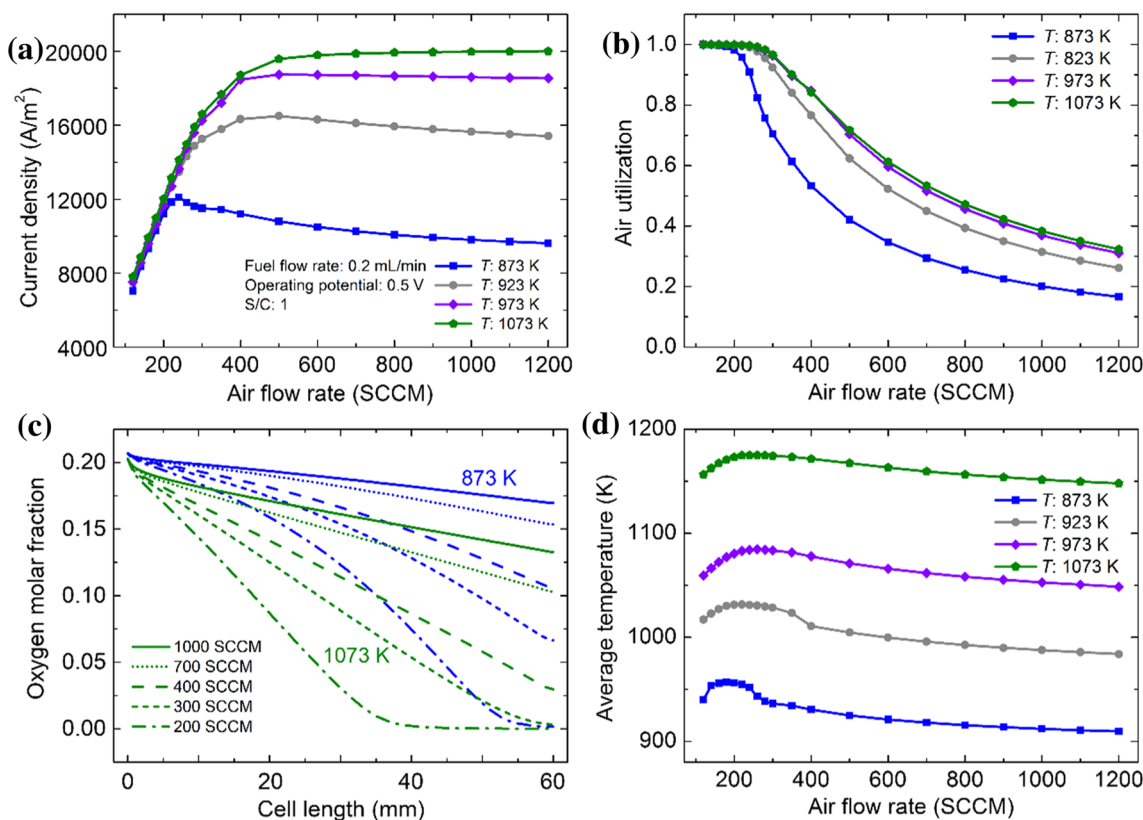
Fig. 2 Effects of the air flow rate on **a** current density; **b** air utilization; **c** oxygen molar fraction distributions along the cell length at the middle of the cathode; **d** anode–electrolyte–cathode average temperature at different temperatures

current density is only about 11,000 A/m² at the air flow rate of 200 SCCM, the temperature gradient still reaches 43.5 K/cm because of poor heat convection and easy heat accumulation. Fortunately, with the rising air flow rate and enhanced flow convective heat transfer capacity, the temperature gradient can be effectively suppressed within 20 K/cm, thus reducing the possibility of structural failure during practical SOFC operation. Besides, the reduction in current density

also plays a role in controlling the high-temperature gradient (Fig. 2a), especially at a high air flow rate, since various heat sources strongly depend upon the current density. Unlike the distribution at 873 K, the largest axial temperature gradient likely exists near the fuel inlet when the fuel cell is operating at 1073 K (Fig. 3b), primarily because the high operating temperature benefits the generation of direct fuels (hydrogen and carbon monoxide), electrochemical reactions, and YSZ
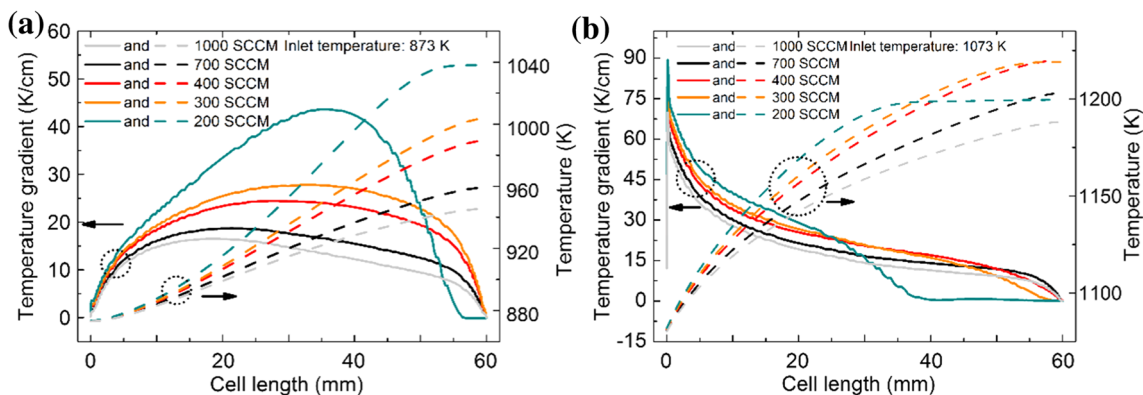
Fig. 3 Effects of the air flow rate on axial temperature gradient and temperature distributions at the middle of the electrolyte at **a** 873 K and **b** 1073 K

electrolyte ion transport, resulting in an extremely elevated current density and thus a huge temperature rise near the fuel inlet (Fig. 3b). Although the increased air flow rate ensures sufficient oxygen supplement (Fig. 2c) and enhanced power generation (Fig. 2a), the induced strong heat convection still promotes heat dissipation under 1073 K, slightly improving the temperature uniformity and reducing the peak temperature gradient.

As the air flow rate continuously increases, mitigations of high temperature and peak temperature gradient become negligible for both operating temperature conditions (Fig. 3a and b), indicating that heat convective capacity arising from the air flow can show a limited cooling effect on the exothermic cell when the air flow rate exceeds a certain value. Therefore, to better evaluate the effectiveness of this active cooling strategy, an excess air ratio is introduced to represent the actual air flow rate [26]. As observed in Fig. 4, all peak temperature gradients occur in two stages with the increase in excess air ratio (air flow rate: 200–2400 SCCM), involving sudden and then gradual declines. At 1073 K, tripling the air ratio from 2 to 6 merely results in about an 18% reduction in the maximum temperature gradient, indicating that the local high-temperature gradient cannot be efficiently eliminated to a safe value (less than 10 K/cm [15, 19]) by simply increasing the airflow rate at such a high current density (0.5 V), especially for high-temperature conditions, which is consistent with Promsen's statement [26]. The underlying reason for the airflow's poor cooling effect could be the restricted heat convection between the cell assembly and the convective gas flow in the air channel, as evidenced by the heat transfer mechanism at the cathode [35]. Unlike the anode, where the heat generated from the thin interface is principally transported by mass transfer. Since the convective flow resulting from the mass exchange moves away from the anode functional layer [60], heat conduction serves as the predominant form of heat transfer in the cathode as the air flows toward the cathode functional layer. Besides, the reported dimensionless value of π_z, a parameter comparing heat convection with conduction, is 1.075 for the anode,
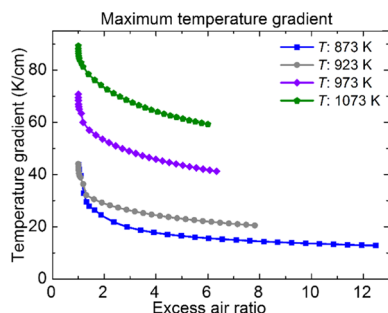
three orders higher as that for the cathode. Therefore, simply accelerating the convective flow in the air channel is not the most effective strategy to control temperature and temperature gradient within the safe region. Besides, an additional air flow normally increases the cost [59] since, reportedly, over 10% of the total cell electricity generation will be consumed by the air blower devices [16, 21, 61]. Therefore, the air flow rate must be carefully controlled considering material deterioration, structural integrity, and cell efficiency.

Effects of Operating Potential

As the key factor, the operating potential can have a dramatic effect on the cell's thermal characteristics. The effects of operating potential at different temperatures are illustrated in Fig. 5. Due to the endothermic MDR, the electrolyte temperature initially decreases and subsequently increases because of the synergistic promotional effects between local current density and actual cell temperature downstream. A local cooling spot near the gas inlet results in an abrupt fall of the axial temperature gradient, especially at a relatively high operating potential (Fig. 5a, b). The low localized temperature could negatively influence the current density (Fig. 5c, d), contributing little to the cell's electrical performance, and the induced temperature gradient (−60 K/cm) does not fall within the safe region for a long-term stable operation based on the recommendation value (10 K/cm) of maximum temperature gradient [15, 19], thus increasing the failure possibility related to the structural defects, such as cracks and delamination due to the applied thermal stress on the brittle ceramic structure. Fortunately, the peak temperature gradient caused by the internal reforming operation could be effectively inhibited by properly adjusting the operating potential as a free condition of extremely high positive or negative peak temperature gradient could be achieved between 0.5 and 0.6 V at 873 K, and 0.6 and 0.7 V at 1073 K (Fig. 5a, b), thereby achieving a localized thermal neutral state. Therefore, an abnormal temperature gradient could be avoided by selecting suitable operating conditions for the fuel cell without sacrificing significant power generation since excessive heat generated from the cell's inefficiency could be consumed by the endothermic decomposition reaction, showing an efficient and attractive operation of direct internal reforming in an SOFC.

In addition, temperature reduction near the cell inlet induced by the MDR could also be affected. A higher operating temperature and a lower potential favor the decomposition reaction (Fig. 6a), mainly arising from the higher reaction kinetics and promotional effects of hydrogen and carbon monoxide consumption by the faradic processes, respectively. Despite the high average current density at a high working temperature, a more favored endothermic reaction leads to a large temperature drop at the operating
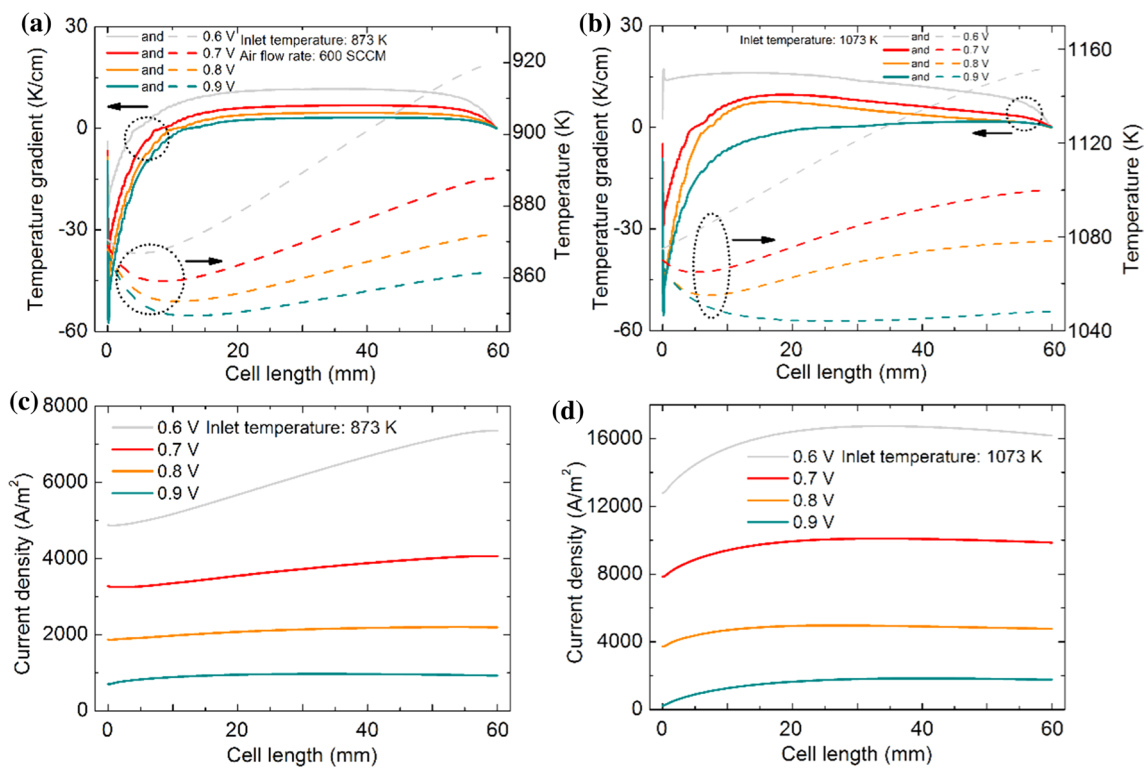

Fig. 4 Effect of excess air ratio on the maximum axial temperature gradient at the middle of the electrolyte under different temperatures

Fig. 5 **a**, **b** Effects of operating potential on axial temperature gradient and temperature; **c**, **d** local current density distributions at the middle of the electrolyte under different temperatures of **a**, **c** 873 K and **b**, **d** 1073 K

potential of 0.9 V (Fig. 6b). Moreover, contrary to the published fact that cells operated on methane fuel generally experience large temperature drops, a relatively lower temperature reduction (below 30 K) is found in the present model, as demonstrated in Fig. 7. Dokmaingam et al. [62] have drawn a similar conclusion that methanol-fueled IIR-SOFC (indirect internal reforming) provided the smoothest temperature change among various promising fuels, including methane,

biogas, methanol, and ethanol. The potential reason is related to different thermodynamical intensities of internal reforming reactions. Within the actual working temperature of SOFC (from 1000 to 1200 K), MDR is moderately endothermic as the associated reaction heat consumption is about 105 kJ/mol, while methane steam (226 kJ/mol) and dry (260 kJ/mol) reforming processes are highly endothermic [40, 42]. Therefore, compared to methane reforming reactions, MDR
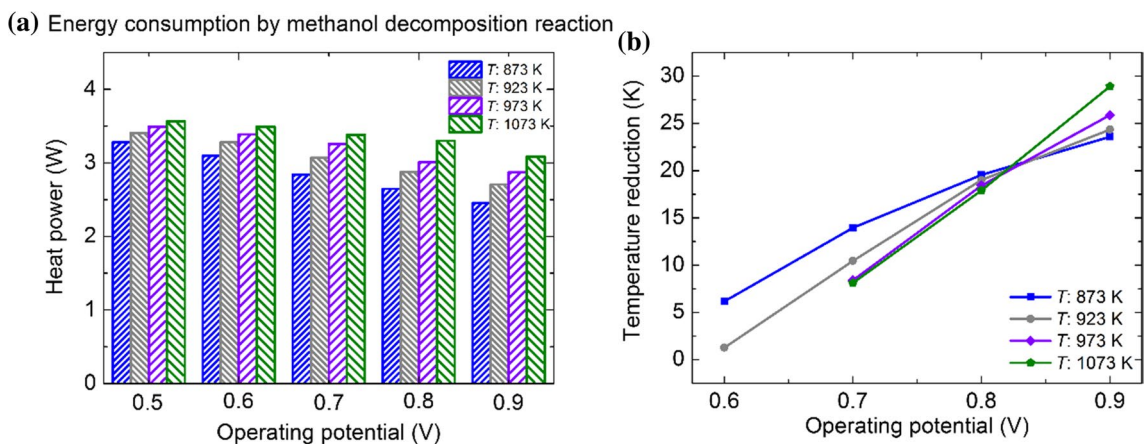
Fig. 6 Effects of operating potential on **a** energy consumption via the endothermic methanol decomposition reaction; **b** maximum temperature reduction at the middle of the electrolyte under different temperatures
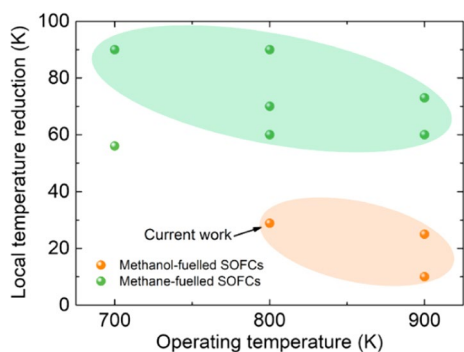
Fig. 7 Comparison of local temperature reduction due to the internal reforming reactions between methanol and methane-fueled SOFCs. Data from Ref. [2, 15, 42, 62, 68–70]

Fig. 8 Effect of air temperature increment on the electrochemical performance and the average temperature of anode–electrolyte–cathode at 973 K and 1073 K

is less endothermic and could lead to a lower temperature drop, which is beneficial to cell performance and durability, especially while operating under a start-up or partial load condition, showing a promising prospect for methanol as the fuel for SOFCs from a thermodynamic perspective.

Effects of Air Inlet Temperature

Besides the cathode gas flow rate, the air inlet temperature can also influence the cell performance and thermal features. Therefore, the effects of cathode gas temperature are studied at the fuel gas inlet temperatures of 973 and 1073 K.

With the rising air inlet temperature, the calculated current densities increase because of the increased average temperature of the cell assembly, as shown in Fig. 8. Besides, the current density at 973 K experiences a larger improvement than that at 1073 K because of higher cell sensitivity to temperature change, as demonstrated previously. Surprisingly, a small amount of air temperature increment can decrease the peak axial temperature gradient of the electrolyte near the inlet to some extent (Fig. 9a, b). For example, increasing the air temperature by 5 K could reduce the temperature gradients by about 18% for 973 K and 20% for 1073 K. However, with a further increase, a negative peak temperature gradient can appear because of the newly generated low-temperature spot, especially for the large air temperature increment. The reduction in the peak temperature gradient is due to the warmer air flow serving as the heat source to heat the front end of the cell assembly, which could lead to a gradual temperature increase at the corresponding position (Fig. 9a, b), smoothing the temperature gradient distribution. In contrast, the excessively warmer air flow could cause a low-temperature spot because of the heat transfer between the air stream and the cell assembly when the temperature difference becomes larger than 30 K, creating a new negative peak temperature gradient. Meanwhile, a comparable positive peak temperature gradient could also be formed at
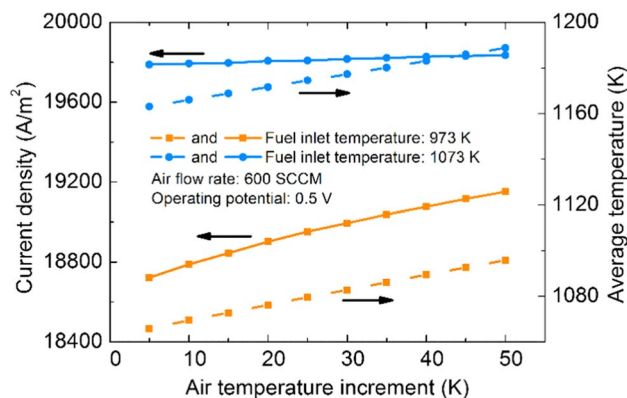
the subsequent position at 973 K, and this is mainly because of the enhanced local current density upstream (Fig. 9c). Besides, low molar fractions of effective fuels at the anode (Fig. 9d) due to the improved cell performance cause a more rapid drop in the local current density downstream for the high increment of air temperature (Fig. 9c), thus lowering the heat generation and subsequently, the temperature gradient. Compared to the condition of 973 K, the cell with a fuel inlet temperature of 1073 K controls the temperature gradient more optimally since a minimal air temperature increase could lead to more temperature gradient reduction, and a further increment could not result in either huge negative or positive gradients because of a higher current density and reduced cell sensitivity to temperature change, respectively.

However, the increase in the air inlet temperature can have a complicated effect on the temperature gradients of other components (Fig. 10). Given the anode-supported structure used in this model, an increased air temperature increases the temperature gradient for the anode mainly because of a relatively long distance to the air channel and enhanced exothermic processes. Conversely, a larger gradient drop could be observed at the cathode since it is the component with the shortest distance to the air channel.

In general, simply increasing the temperature of the incoming air could help reduce the peak temperature gradient of the electrolyte and thus the structural failure possibility since it is frequently reported that the maximum tensile stress can exist in the electrolyte of SOFC, especially for the internal reforming operation [27–29, 63, 64], practically making the electrolyte the most vulnerable component. However, the negative effects of this approach on other important components must be paid attention to as there is a trade-off in the temperature gradient changes at different radial positions.
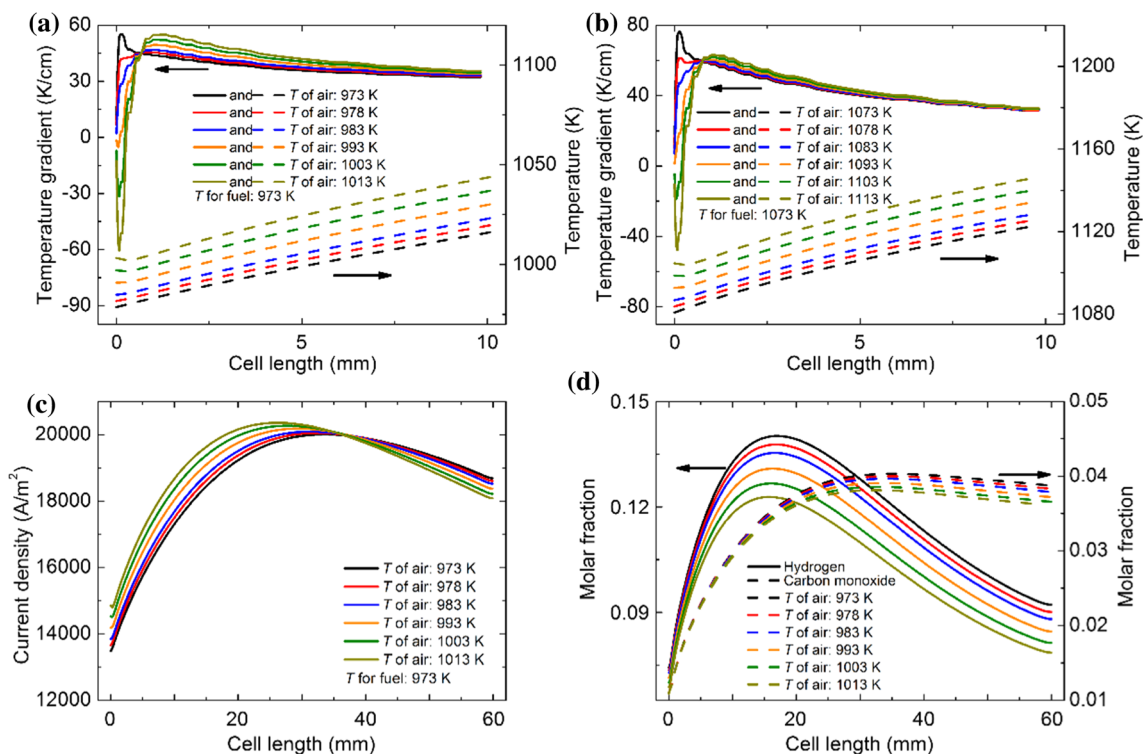
Fig. 9 Effects of air temperature increment on the axial temperature and temperature gradient distributions at the middle of the electrolyte at **a** 973 K and **b** 1073 K in the cell's upstream (0 to 10 mm); **c** local current density distribution along the cell length; **d** molar fractions of H_2 and CO along the cell length at the middle of anode under the fuel inlet temperature of 973 K
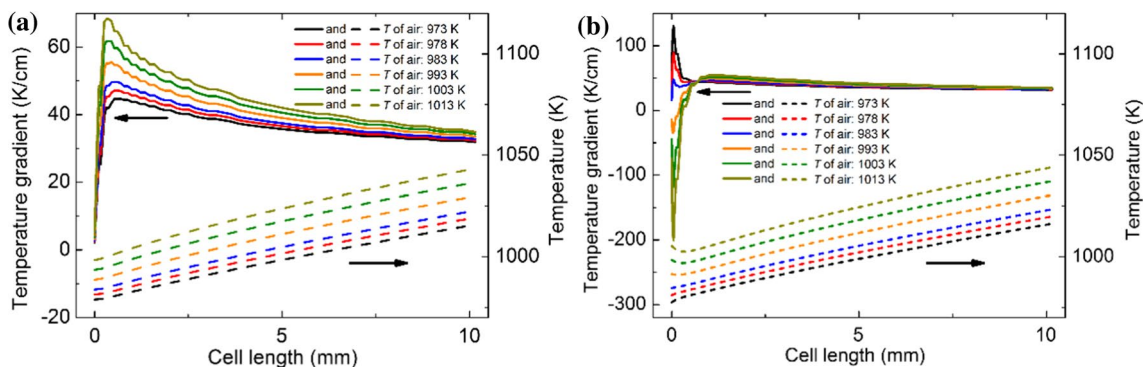

Fig. 10 Effects of air temperature increment on axial temperature and temperature gradient distributions at the middle of the **a** anode and **b** cathode in the cell's upstream (0 to 10 mm) at 973 K

Effects of Fuel/Air Flow Arrangements

Flow arrangements of the tubular fuel cell, including co-flow and counter-flow are critically important to its electrochemical characteristics and thermal management (Table 4); thus, cells with different air flow directions are simulated to assess the heat dissipation capacity at 973 K and 0.5 V. As indicated in Fig. 11, a distinctive discrepancy of temperature distributions is that a cell with a counter-flow setup exhibits a larger high-temperature area compared to the co-flow counterpart, especially in the fuel inlet region where the reforming reaction is primarily performed, thus producing more effective fuels for faradic processes, indicating a more efficient waste heat recovery for the endothermic decomposition reaction. Besides, a considerably higher average cell assembly temperature of 1102.4 K enables the counter-flow cell to perform better, leading to a higher current density
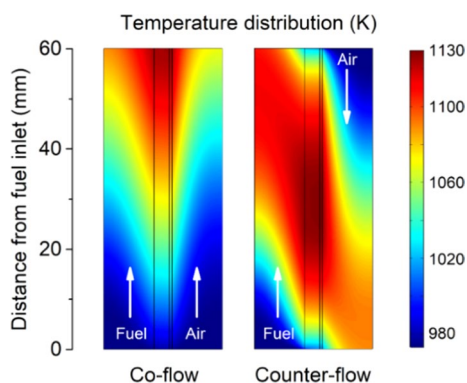
Fig. 11 Distributions of cell temperature of different flow arrangements at 973 K

Table 4 Comparison of the cell thermal and electrochemical characteristics between different flow arrangements at 973 K

Properties	Co-flow	Counter-flow
Current density (A/m²)	18,722	19,878
Maximum temperature (K)	1125.5	1129.4
Minimum temperature (K)	978.63	1014.4
Average temperature (K)	1066.4	1102.4
Maximum temperature gradient (K/cm)	57.45	− 382.58/136.66

(Table 4). Therefore, the cell with the counter-flow arrangement is characterized by higher power output and thereby efficiency, which coincides with many research works [15, 29, 58, 65–67] from literature. However, a large high-temperature area is generated by the poor heat dissipation because opposite directions of air and fuel flows diminish

the heat convection capacity, causing heat accumulation near the cell center.

Quite different temperature distributions between these two configurations can create much disparate temperature gradient distributions, as demonstrated in Fig. 12. In addition to a higher positive peak gradient (136.66 K/cm) near the fuel inlet, a negative one (− 382.58 K/cm) is also found near the air inlet for the counter-flow setting because the axial temperature can decrease from the cell center (Fig. 12b) due to the combined effects of the cooler incoming air and the decreased local current density (Fig. 12c) evident from the
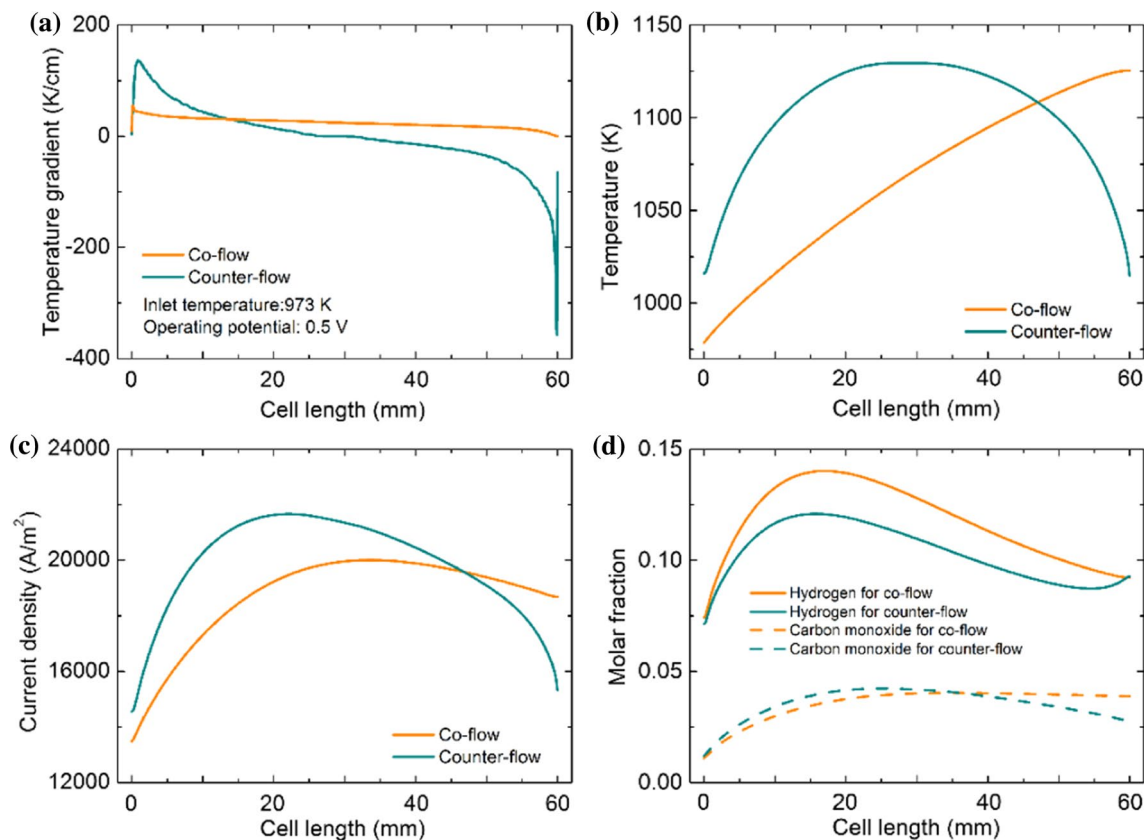

Fig. 12 **a** Axial temperature gradient, **b** temperature, and **c** current density distributions of different flow arrangements along the cell length at the middle of the electrolyte; **d** molar fractions of H₂ and CO along cell length at the middle of the anode under 973 K

slight increase in hydrogen fuel near the air inlet (Fig. 12d). Notably, the absolute value of the negative peak gradient is much higher than that of the positive one, mainly because the rate of temperature drop at the air inlet is higher compared to the temperature rising rate near the fuel inlet due to the anode-supported structure used in the current model and the more rapid drop of current density near the air inlet than the current density enhancement near fuel inlet (Fig. 12c). Therefore, the co-flow configuration has a safer temperature profile, while much higher temperature gradients are found in both fuel and air inlets for the counter-flow counterpart.

Radial temperature and temperature gradient distributions of the cell assembly have not been discussed frequently due to negligible temperature variation along the thickness direction since relatively high thermal conductivities enable solid materials to conduct heat efficiently. For the co-flow arrangement, the radial temperature difference is less than 1 K (Fig. 13) because fuel and air flows follow the same temperature variation pattern, leading to relatively small temperature gradients at three typical positions (Fig. 14). However, the temperature along the cell thickness exhibits different tendencies at different axial positions for the counter-flow setting (Fig. 13), showing opposite temperature changes at the fuel and air inlets. Besides, a relatively high gradient intensity (-60.5 K/cm) could be found at the interface of electrolyte and cathode near the air inlet (fuel outlet) (Fig. 14a), again because anode supportive structure enables the electrolyte to dissipate heat more rapidly through the thin cathode near the air inlet.
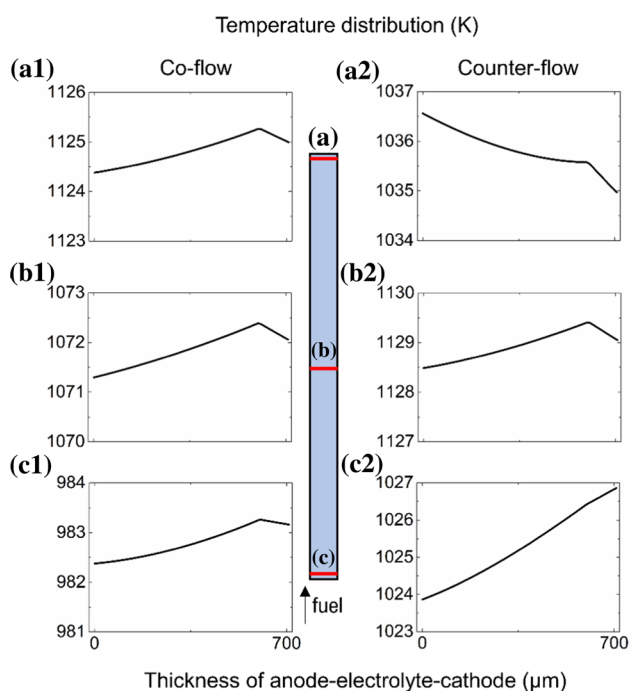
Conclusion

The two-dimensional axisymmetric model studies the thermal and electrochemical characteristics of tubular SOFC fed by equimolar amounts of methanol and steam. This validated numerical model fully considers the mass and heat transfer processes, hydrogen/carbon monoxide electrochemical oxidations, as well as methanol conversion and simulates the cell's thermo–fluid environment under various working conditions involving operating potential, air flow rate inlet temperature, and gas flow arrangements. The main conclusions are as follows:

(1) The air flow rate can have a complicated effect on a cell's performance. Limited by the insufficient oxygen at relatively low air flow rates, current densities increase dramatically with the rising air flow rate. However, with a further increase, the power output experiences a gradual drop because of the induced temperature decrease at 873, 923, and 973 K, but a slight increase at 1073 K due to the low cell sensitivity to temperature variation. Besides, as an active cool-
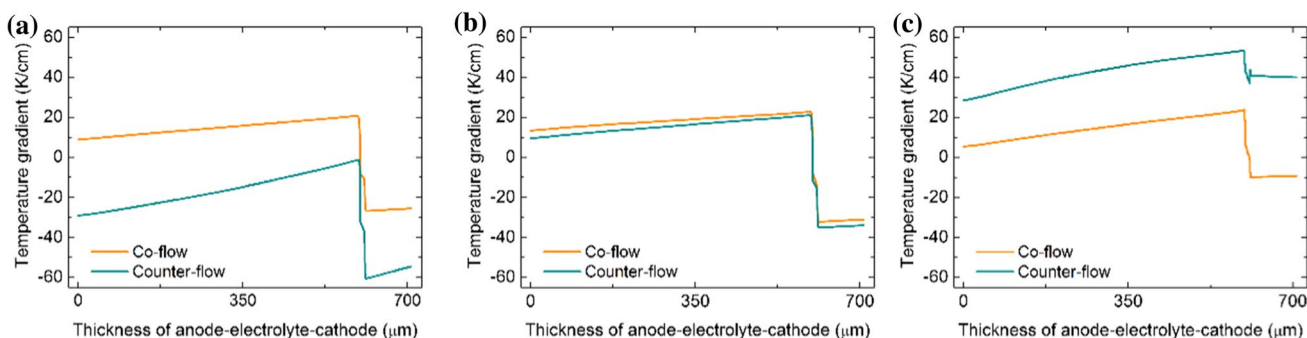

Fig. 13 Radial temperature distributions at three positions of the cell under 973 K (**a** 59 mm, **b** 30 mm, and **c** 1 mm from fuel inlet)

Fig. 14 Radial temperature gradient distributions at three positions of the cell at 973 K (**a** 59 mm, **b** 30 mm, and **c** 1 mm from fuel inlet)

ing strategy, oversupplying the cathode air could not effectively suppress the detrimental thermal features to a safe level at a considerably high current density due to the intrinsic heat transfer in the cathode.

(2) Owing to the thermal coupling of cell inefficiencies and the endothermic decomposition reaction, a localized thermal neutral state was achieved by suitably adjusting the operating potential and eliminating the peak axial temperature gradient of the electrolyte. Compared to methane-fueled SOFCs, an SOFC operating on methanol experiences a less temperature reduction (below 30 K) near the fuel inlet due to the less endothermic thermodynamic nature, causing fewer negative effects on the cell performance and durability.

(3) Interestingly, increasing the air inlet temperature by 5 K could suppress the peak axial temperature gradients by about 18% at 973 K and 20% at 1073 K since warmer fresh air can be the heat source to heat the front end of the fuel cell, while a further increase could generate negative and positive temperature gradient peaks because of the new cooling spot and elevated current density, respectively. However, as the result of the anode's supportive structure, an increased air inlet temperature can have different effects on other components, thus increasing the corresponding failure possibility.

(4) Unlike the cell with the co-flow arrangement, high temperature concentrates at the cell center for the counter-flow counterpart, enhancing the electricity output and cell efficiency. However, because of poor heat dissipation capacity and enhanced heat generation, the cell with the counter-flow setting is characterized by higher local temperature gradients along the cell length and radial direction, making the counter-flow undesirable from the perspective of thermal stability.

Notably, in addition to the temperature gradient distribution, mechanical properties of cell components, including thermal expansion coefficient, elasticity, and Poisson's ratio, can affect the cell's thermal stress conditions. Therefore, the electro–thermo–mechanical modeling of SOFCs is considered in our subsequent simulation work to study the operation stability related to thermal stress.

Declarations

Conflict of interest The authors declare that there is no conflict of interest.

References

1. Singhal SC, Kendall K (2002) High-temperature solid oxide fuel cells: fundamentals, design and applications. Mater Today 5(12):55

2. Ni M (2011) Electrolytic effect in solid oxide fuel cells running on steam/methane mixture. J Power Sources 196(4):2027–2036

3. Jiao K, Xuan J, Du Q et al (2021) Designing the next generation of proton-exchange membrane fuel cells. Nature 595(7867):361–369

4. Garcia-Garcia FJ, Yubero F, González-Elipe AR et al (2018) Microstructural engineering and use of efficient poison resistant Au-doped Ni-GDC ultrathin anodes in methane-fed solid oxide fuel cells. Int J Hydrog Energy 43(2):885–893

5. Garcia-Garcia FJ, Beltrán AM, Yubero F et al (2017) High performance novel gadolinium doped ceria/yttria stabilized zirconia/nickel layered and hybrid thin film anodes for application in solid oxide fuel cells. J Power Sources 363:251–259

6. Wang W, Su C, Wu YZ et al (2013) Progress in solid oxide fuel cells with nickel-based anodes operating on methane and related fuels. Chem Rev 113(10):8104–8151

7. Su HR, Hu YH (2020) Progress in low-temperature solid oxide fuel cells with hydrocarbon fuels. Chem Eng J 402:126235

8. Wang W, Qu JF, Julião PSB et al (2019) Recent advances in the development of anode materials for solid oxide fuel cells utilizing liquid oxygenated hydrocarbon fuels: a mini review. Energy Technol 7(1):33–44

9. Ni M (2011) Thermo-electrochemical modeling of ammonia-fueled solid oxide fuel cells considering ammonia thermal decomposition in the anode. Int J Hydrog Energy 36(4):3153–3166

10. Afif A, Radenahmad N, Cheok Q et al (2016) Ammonia-fed fuel cells: a comprehensive review. Renew Sustain Energy Rev 60:822–835

11. Radenahmad N, Azad AT, Saghir M et al (2020) A review on biomass derived syngas for SOFC based combined heat and power application. Renew Sustain Energy Rev 119:109560

12. Jiang CR, Ma JJ, Corre G et al (2017) Challenges in developing direct carbon fuel cells. Chem Soc Rev 46(10):2889–2912

13. Cao TY, Huang K, Shi YX et al (2017) Recent advances in high-temperature carbon–air fuel cells. Energy Environ Sci 10(2):460–490

14. Xu QD, Guo ZJ, Xia LC et al (2022) A comprehensive review of solid oxide fuel cells operating on various promising alternative fuels. Energy Convers Manag 253:115175

15. Aguiar P, Adjiman CS, Brandon NP (2004) Anode-supported intermediate temperature direct internal reforming solid oxide fuel cell. I: model-based steady-state performance. J Power Sources 138(1–2):120–136

16. Dillig M, Plankenbühler T, Karl J (2018) Thermal effects of planar high temperature heat pipes in solid oxide cell stacks operated with internal methane reforming. J Power Sources 373:139–149

17. Palomba V, Ferraro M, Frazzica A et al (2018) Experimental and numerical analysis of a SOFC-CHP system with adsorption and hybrid chillers for telecommunication applications. Appl Energy 216:620–633

18. Hosseinpour J, Sadeghi M, Chitsaz A et al (2017) Exergy assessment and optimization of a cogeneration system based on a solid oxide fuel cell integrated with a stirling engine. Energy Convers Manag 143:448–458

19. Zeng ZZ, Qian YP, Zhang YJ et al (2020) A review of heat transfer and thermal management methods for temperature gradient reduction in solid oxide fuel cell (SOFC) stacks. Appl Energy 280:115899

20. Hubert M, Laurencin J, Cloetens P et al (2018) Impact of nickel agglomeration on solid oxide cell operated in fuel cell and electrolysis modes. J Power Sources 397:240–251

21. Zeng HY, Wang YQ, Shi YX et al (2018) Highly thermal integrated heat pipe-solid oxide fuel cell. Appl Energy 216:613–619

22. Zhang T, Zhu QS, Huang WL et al (2008) Stress field and failure probability analysis for the single cell of planar solid oxide fuel cells. J Power Sources 182(2):540–545

23. Dikwal CM, Bujalski W, Kendall K (2009) The effect of temperature gradients on thermal cycling and isothermal ageing of micro-tubular solid oxide fuel cells. J Power Sources 193(1):241–248

24. Boldrin P, Brandon NP (2019) Progress and outlook for solid oxide fuel cells for transportation applications. Nat Catal 2(7):571–577

25. Marocco P, Ferrero D, Lanzini A et al (2019) Benefits from heat pipe integration in H_2/H_2O fed SOFC systems. Appl Energy 241:472–482

26. Promsen M, Komatsu Y, Sciazko A et al (2020) Feasibility study on saturated water cooled solid oxide fuel cell stack. Appl Energy 279:115803

27. Wang YQ, Ren JW, Shi YX et al (2019) Numerical model of direct internal reforming SOFC: a comparison between anode-support and metal-support. ECS Trans 91(1):2013–2022

28. Ren JW, Wang YQ, Shi YX (2022) Numerical simulation and thermal stress analysis of direct internal reforming SOFCs. Int J Green Energy 19(4):399–409

29. Selimovic A, Kemm M, Torisson T et al (2005) Steady state and transient thermal stress analysis in planar solid oxide fuel cells. J Power Sources 145(2):463–469

30. Zhan RB, Wang Y, Ni M et al (2020) Three-dimensional simulation of solid oxide fuel cell with metal foam as cathode flow distributor. Int J Hydrog Energy 45(11):6897–6911

31. Park J, Kim YM, Bae J (2011) A numerical study on the heat and mass transfer characteristics of metal-supported solid oxide fuel cells. Int J Hydrog Energy 36(4):3167–3178

32. Tucker MC (2010) Progress in metal-supported solid oxide fuel cells: a review. J Power Sources 195(15):4570–4582

33. Tucker MC (2017) Development of high power density metal-supported solid oxide fuel cells. Energy Technol 5(12):2175–2181

34. Dogdibegovic E, Wang RF, Lau GY et al (2019) High performance metal-supported solid oxide fuel cells with infiltrated electrodes. J Power Sources 410–411:91–98

35. Lee S, Park M, Kim H et al (2017) Thermal conditions and heat transfer characteristics of high-temperature solid oxide fuel cells investigated by three-dimensional numerical simulations. Energy 120:293–305

36. Xu QD, Xia LC, He QJ et al (2021) Thermo-electrochemical modelling of high temperature methanol-fuelled solid oxide fuel cells. Appl Energy 291:116832

37. Xu QD, Ni M (2021) Modelling of high temperature direct methanol solid oxide fuel cells. Int J Energy Res 45(2):3097–3112

38. Jiang Y, Virkar AV (2001) A high performance, anode-supported solid oxide fuel cell operating on direct alcohol. J Electrochem Soc 148(7):A706

39. Palo DR, Dagle RA, Holladay JD (2007) Methanol steam reforming for hydrogen production. Chem Rev 107(10):3992–4021

40. Cimenti M, Hill J (2009) Direct utilization of liquid fuels in SOFC for portable applications: challenges for the selection of alternative anodes. Energies 2(2):377–410

41. Zheng KQ, Sun Q, Ni M (2013) Local non-equilibrium thermal effects in solid oxide fuel cells with various fuels. Energy Technol 1(1):35–41

42. Ni M (2013) Modeling and parametric simulations of solid oxide fuel cells with methane carbon dioxide reforming. Energy Convers Manag 70:116–129

43. Mizsey P, Newson E, Truong TB et al (2001) The kinetics of methanol decomposition: a part of autothermal partial oxidation to produce hydrogen for fuel cells. Appl Catal A Gen 213(2):233–237

44. Haberman BA, Young JB (2004) Three-dimensional simulation of chemically reacting gas flows in the porous support structure of an integrated-planar solid oxide fuel cell. Int J Heat Mass Transf 47(17–18):3617–3629

45. Xu HR, Chen B, Zhang HC et al (2017) The thermal effect in direct carbon solid oxide fuel cells. Appl Therm Eng 118:652–662

46. Chen B, Xu HR, Tan P et al (2019) Thermal modelling of ethanol-fuelled solid oxide fuel cells. Appl Energy 237:476–486

47. Ni M (2013) 2D heat and mass transfer modeling of methane steam reforming for hydrogen production in a compact reformer. Energy Convers Manag 65:155–163

48. Chen B, Xu HR, Zhang HC et al (2017) A novel design of solid oxide electrolyser integrated with magnesium hydride bed for hydrogen generation and storage - a dynamic simulation study. Appl Energy 200:260–272

49. Krishna R, Wesselingh JA (1997) The Maxwell-Stefan approach to mass transfer. Chem Eng Sci 52(6):861–911

50. Veldsink JW, van Damme RMJ, Versteeg GF et al (1995) The use of the dusty-gas model for the description of mass transport with chemical reaction in porous media. Chem Eng J Biochem Eng J 57(2):115–125

51. Evans RB III, Watson GM, Mason EA (1961) Gaseous diffusion in porous media at uniform pressure. J Chem Phys 35(6):2076–2083

52. Todd B, Young JB (2002) Thermodynamic and transport properties of gases for use in solid oxide fuel cell modelling. J Power Sources 110(1):186–200

53. Fuller EN, Ensley K, Giddings JC (1969) Diffusion of halogenated hydrocarbons in helium. The effect of structure on collision cross sections. J Phys Chem 73(11):3679–3685

54. Reid RC, Sherwood TK, Street RE (1959) The properties of gases and liquids. Phys Today 12(4):38–40

55. Luo Y, Shi YX, Li WY et al (2014) Comprehensive modeling of tubular solid oxide electrolysis cell for co-electrolysis of steam and carbon dioxide. Energy 70:420–434

56. Xu HR, Ma JB, Tan P et al (2020) Towards online optimisation of solid oxide fuel cell performance: combining deep learning with multi-physics simulation. Energy AI 1:100003

57. Li YB, Yan HB, Zhou ZF et al (2019) Three-dimensional nonisothermal modeling of solid oxide fuel cell coupling electrochemical kinetics and species transport. Int J Energy Res 43(13):6907–6921

58. Colpan CO, Hamdullahpur F, Dincer I (2011) Transient heat transfer modeling of a solid oxide fuel cell operating with humidified hydrogen. Int J Hydrog Energy 36(17):11488–11499

59. Raj A, Sasmito AP, Shamim T (2015) Numerical investigation of the effect of operating parameters on a planar solid oxide fuel cell. Energy Convers Manag 90:138–145

60. Lee S, Kim H, Yoon KJ et al (2016) The effect of fuel utilization on heat and mass transfer within solid oxide fuel cells examined by three-dimensional numerical simulations. Int J Heat Mass Transf 97:77–93

61. Fardadi M, McLarty DF, Jabbari F (2016) Investigation of thermal control for different SOFC flow geometries. Appl Energy 178:43–55

62. Dokmaingam P, Assabumrungrat S, Soottitantawat A et al (2010) Modelling of tubular-designed solid oxide fuel cell with indirect internal reforming operation fed by different primary fuels. J Power Sources 195(1):69–78

63. Severson H, Assadi M (2013) Analysis of residual and operational thermal stresses in a planar SOFC. J Fuel Cell Sci Technol 10(6):1–14

64. Xu M, Li TS, Yang M et al (2016) Modeling of an anode supported solid oxide fuel cell focusing on thermal stresses. Int J Hydrog Energy 41(33):14927–14940

65. Russner N, Dierickx S, Weber A et al (2020) Multiphysical modelling of planar solid oxide fuel cell stack layers. J Power Sources 451:227552

66. Wang Y, Zhan RB, Qin YZ et al (2018) Three-dimensional modeling of pressure effect on operating characteristics and performance of solid oxide fuel cell. Int J Hydrog Energy 43(43):20059–20076

67. Wongchanapai S, Iwai H, Saito M et al (2012) Selection of suitable operating conditions for planar anode-supported direct-internal-reforming solid-oxide fuel cell. J Power Sources 204(15):14–24

68. Dokamaingam P, Assabumrungrat S, Soottitantawat A et al (2009) Effect of operating conditions and gas flow patterns on the system performances of IIR-SOFC fueled by methanol. Int J Hydrog Energy 34(15):6415–6424

69. Iwai H, Yamamoto Y, Saito M et al (2011) Numerical simulation of intermediate-temperature direct-internal-reforming planar solid oxide fuel cell. Energy 36(4):2225–2234

70. Ho TX, Kosinski P, Hoffmann AC et al (2009) Numerical analysis of a planar anode-supported SOFC with composite electrodes. Int J Hydrog Energy 34(8):3488–3499

71. He QJ, Yu J, Xu HR et al (2020) Thermal effects in H_2O and CO_2 assisted direct carbon solid oxide fuel cells. Int J Hydrog Energy 45(22):12459–12475

72. Wiranarongkorn K, Banerjee A, Deutschmann O et al (2020) Performance analysis and temperature gradient of solid oxide fuel cell stacks operated with bio-oil sorption-enhanced steam reforming. Int J Hydrog Energy 45(21):12108–12120

Dr. Keqing Zheng received her Ph.D. from the Hong Kong Polytechnic University in March 2016. Then, she joined China University of Mining and Technology in July 2016 and was promoted to associate professor in December 2019. Dr. Zheng's research interests include fuel cell modeling, thermal management of fuel cell, and fuel cell-based co-generation systems.

Prof. Meng Ni received his Ph.D. from University of Hong Kong in 2007. Then, Prof. NI joined the Hong Kong Polytechnic University in July 2009 and was promoted to associate professor in July 2012 and then full professor and Associate Head (Research) in July 2016. He was appointed as Associate Dean of Faculty of Construction and Environment in July 2021. Prof. Ni conducted collaboration research at the Forschungszentrum Jülich, Germany in 2017, as a Humboldt Fellow. His research interests include fuel cells, rechargeable metal-air batteries, electrochemical water-splitting and electrochemical systems for low-grade waste heat utilization. Prof. Ni is serving as an active reviewer for over 80 academic journals including Science, Nature Communications, Joule, Advanced Materials etc. He served as Associate Editor for Science Bulletin in 2015–2017. Currently, he is a Senior Editor for Sustainable Energy Technologies and Assessments (Elsevier) and e-Prime (Elsevier) and an Associate Editor for International Journal of Green Energy (Taylor & Francis) and International Journal of Energy Research (Wiley).